

## Direct Evidence of Klein and Anti-Klein Tunneling of Graphitic Electrons in a Corbino Geometry


Mirza M. Elahi<sup>1,\*</sup>, Hamed Vakili<sup>2</sup>, Yihang Zeng<sup>3,†</sup>, Cory R. Dean<sup>3</sup>, and Avik W. Ghosh<sup>1,4</sup>

<sup>1</sup>*Department of Electrical and Computer Engineering, University of Virginia, Charlottesville, Virginia 22904, USA*

<sup>2</sup>*Department of Physics and Astronomy and Nebraska Center for Materials and Nanoscience, University of Nebraska, Lincoln, Nebraska 68588, USA*

<sup>3</sup>*Department of Physics, Columbia University, New York, New York 10027, USA*

<sup>4</sup>*Department of Physics, University of Virginia, Charlottesville, Virginia 22904, USA*

 (Received 6 June 2023; revised 10 October 2023; accepted 1 February 2024; published 2 April 2024)

Transport measurement of electron optics in monolayer graphene  $p$ - $n$  junction devices has been traditionally studied with negative refraction and chiral transmission experiments in Hall bar magnetic focusing setups. We show direct signatures of Klein (monolayer) and anti-Klein (bilayer) tunneling with a circular “edgeless” Corbino geometry made out of gated graphene  $p$ - $n$  junctions. Noticeable in particular is the appearance of angular sweet spots (Brewster angles) in the magnetoconductance data of bilayer graphene, which minimizes head-on transmission, contrary to conventional Fresnel optics or monolayer graphene which show instead a sharpened collimation of transmission paths. The local maxima on the bilayer magnetoconductance plots migrate to higher fields with increasing doping density. These experimental results are in good agreement with detailed numerical simulations and analytical predictions.

DOI: [10.1103/PhysRevLett.132.146302](https://doi.org/10.1103/PhysRevLett.132.146302)

Topological attributes of 2D Dirac fermions generate electronic properties not easily seen in their optical counterparts, such as a gate tunable negative index of electron refraction [1,2]. Unlike photons, the Dirac cone angle of graphitic electrons is fixed by carbon  $p_z$  orbital hopping, so that electrons must redirect their path at an interface without slowing down [3]. The Bloch part of the electron or hole wave function for an  $N$ -layer Bernal stacked graphene creates a pseudospin that executes  $N$  full rotations around the Fermi surface (Fig. 1) with Berry phase  $N\pi$ . We shortly establish that the corresponding reflectivity at small incident angle  $\theta_i$  across an electrostatically gated  $p$ - $n$  junction varies as  $\sin N\theta_i$  for odd  $N$  and  $\cos N\theta_i$  for even  $N$ , giving alternately perfect head-on transmission [Klein tunneling (KT)] or perfect head-on reflection [anti-Klein tunneling (AKT)]. This universality contrasts with optical counterparts whose low angle reflectivity is set by the fractional change in refractive index. At the same time, higher angle electrons collimate with increasing voltage barrier (refractive index mismatch) across the split-gated junction. By cascading multiple angled junctions, the overall transmission can be quenched much like a polarizer-analyzer pair, for potential use in digital [4,5] and analog electronics [6].

While the electronic analogs of Snell’s law including negative index [2] and Malus’s law [7] have already been seen, experiments showing transmission peaks or KT have only been seen indirectly [2,5,8–12], arguing for a more direct evidence. More striking would be a demonstration of AKT [13], the *minimizing* of transmission at normal

incidence unlike any optical analog, producing a transmission peak at an intermediate, gate tunable incidence precisely analogous to Brewster angles for perpendicular polarized light. Attempts to see this experimentally, such as in Fabry-Perot evolution of Berry phase in bilayer graphene in a planar geometry, revealed similar effects in theory [e.g., Ref. [14], Figs. 3(b) and 3(h)], but no such zero-field dips in experiments [Ref. [14], Figs. 3(a) and 3(g)].

In this Letter, we study magnetotransport in edgeless Corbino disk devices with concentric gated  $p$ - $n$  junctions at fixed radial distance between the inner and outer electrode. Corbino geometries are particularly convenient over Hall bar geometries [2] for their ability to allow small incidence angles, higher mobility, and lower scattering that has allowed us to resolve fractional quantum Hall edge states in graphene [15–19]. For monolayer graphene (MLG), we observe a magnetoconductance peak at zero field (Fig. 2) with clearly suppressed transmission in an  $n$ - $p'$ - $n$  junction compared to  $n$ - $n'$ - $n$ , as expected from our KT simulations with no adjustable parameters. Strikingly, for bilayer graphene (BLG), we see a dip in some of the magnetoconductance traces around zero magnetic field (Fig. 3) consistent with AKT, and a flattened plateau associated with incipient dips in the other traces. The overall evolution of the peaks and shoulders versus doping densities agrees very well with theoretical simulations both semiclassical and fully quantum (see Supplemental Material [20]), serving arguably as direct evidence of KT and AKT in graphene.

*Theoretical background: Klein (anti-Klein) tunneling in monolayer (bilayer) graphene Corbino disk device.—The*

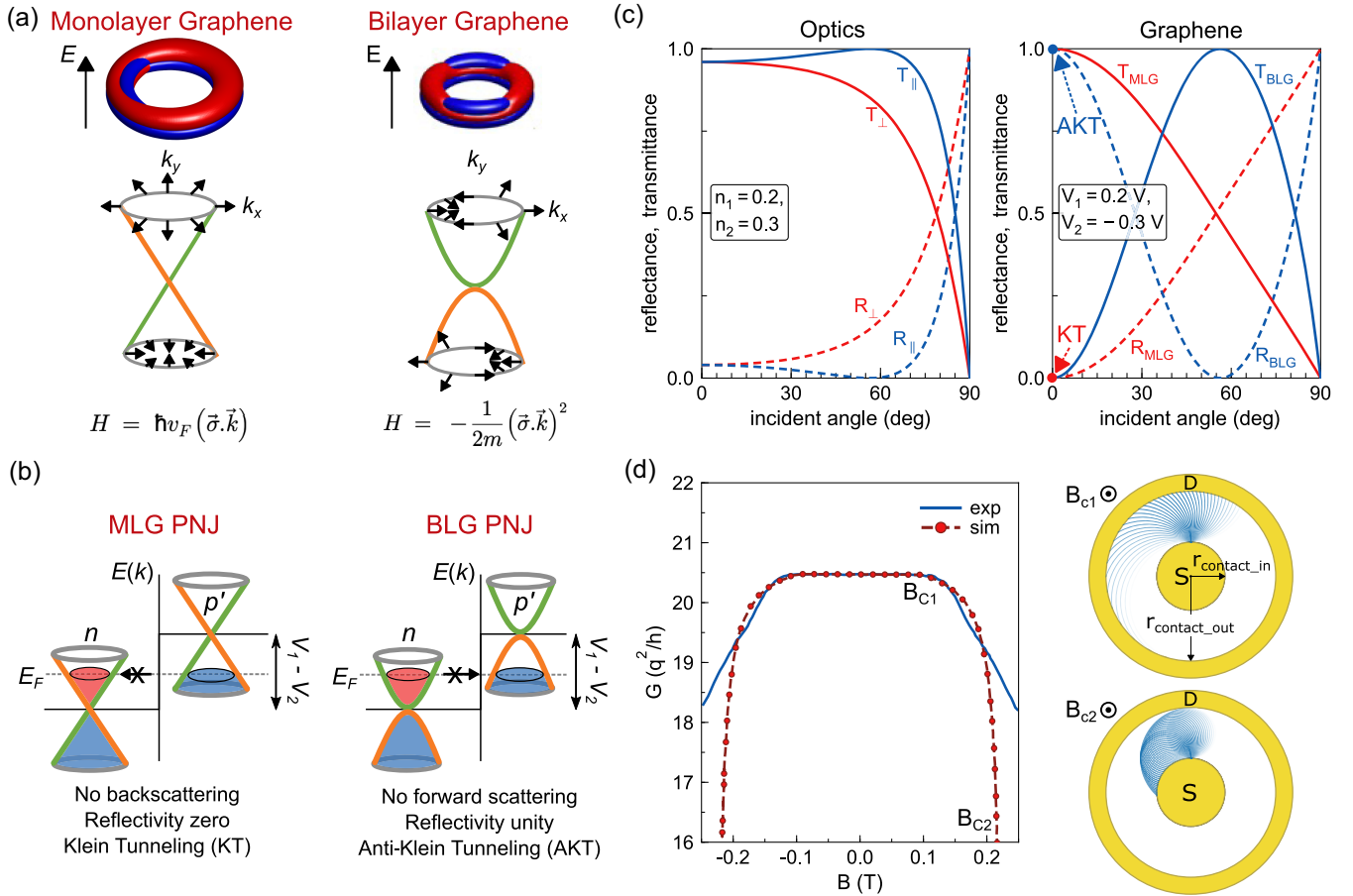


FIG. 1. (a)–(c) Klein or anti-Klein tunneling in layered graphene, compared with optical transmission. (a) Pseudospin evolution around the graphene Fermi surface, with red and blue lobes showing positive and negative lobes of dimer  $p_z$  orbitals. Bilayer graphene (BLG) pseudospins rotate twice as fast as in monolayer graphene (MLG). Orange versus green branches label left-oriented pseudospin (i.e., antibonding dimer  $p_z$  orbitals) versus right-oriented pseudospin (bonding). (b) Schematic of Klein and anti-Klein tunneling at MLG and BLG split gated  $p$ - $n$  junction (PNJ) at normal incidence. (c) Reflectivity  $R$  (dashed line) and transmittivity  $T$  (solid line) of in-plane versus perpendicular (blue  $\parallel$  and red  $\perp$ ) photons across a junction, dictated by Fresnel equations. Electron reflection at a graphene  $p$ - $n$  junction (red dashed line in MLG) shows KT at normal incidence, while in BLG (blue dashed line) it shows AKT at normal incidence as well as a Brewster angle set by  $\tan^{-1}(V_2/V_1)$ , here near  $60^\circ$ , where  $R_{\text{BLG}}$  vanishes. (d) Magnetoconductance plots (solid line experiment, parameters in the text, and dashed line simulation) for junctionless Corbino disk graphene structure that form the basis of our experiments. The cutoff fields  $B_{c1}$  and  $B_{c2}$  are where the electron cyclotron orbits narrowly miss the farthest and nearest access to the outer contact.

low energy electronic band structure for an  $N$ -layer Bernal stacked graphene is given by

$$H = \left( \frac{\hbar v_F}{\gamma} \right)^N \begin{pmatrix} 0 & (\pi^-)^N \\ (\pi^+)^N & 0 \end{pmatrix}, \quad (1)$$

with  $\pi^\pm = (k_x \pm ik_y)/|k| = e^{\pm i\theta}$ . The solutions are spinor-like (“pseudospin”) wave functions,

$$\psi_C = \frac{1}{\sqrt{2}} \begin{pmatrix} 1 \\ e^{iN\theta} \end{pmatrix}, \quad \psi_V = \frac{1}{\sqrt{2}} \begin{pmatrix} 1 \\ (-1)^{N+1} e^{iN\theta} \end{pmatrix}, \quad (2)$$

with  $C$  and  $V$  representing conduction and valence bands respectively. In Fig. 1, the orthogonal states  $(1, \pm 1)/\sqrt{2}$ ,

i.e., the bonding and antibonding combinations of the frontier dimer  $p_z$  orbitals (in plane for MLG, cross-planar for BLG) are colored as green and orange, respectively. The corresponding reflection and transmission coefficients across a junction, obtained by matching the two-component pseudospinors at the interface, are

$$T = 1 - R = \frac{\cos[N(\theta_i + \theta_t)] - (-1)^N \cos[N(\theta_i - \theta_t)]}{1 + \cos[N(\theta_i + \theta_t)]} = \begin{cases} \frac{2 \cos(N\theta_i) \cos(N\theta_t)}{1 + \cos[N(\theta_i + \theta_t)]} & (N \text{ odd}) \\ \frac{2 \sin(N\theta_i) \sin(N\theta_t)}{1 + \cos[N(\theta_i + \theta_t)]} & (N \text{ even}), \end{cases} \quad (3)$$

where the incident and transmitted angles are related by Snell's law,  $\sin \theta_i / \sin \theta_t = V_2 / V_1$ , set by the local gate induced potentials on the transmitted and incident sides ( $\theta_t$  is negative for  $p$ - $n$  junctions with opposite gate polarity). The equations modify a bit for  $|V_1| > |V_2|$  where we have total internal reflection, and for split gates [3] where an additional angle-dependent tunneling prefactor comes in [4], but the overall physics stays intact.

Note that for all odd (even)  $N$ , we get KT (AKT) with perfect transmission (reflection) at  $\theta_i = 0$  (Fig. 1). These universal values are imposed by the topology of the pseudospin, i.e., matching subband colors across the junction. Note also that for even  $N$  we get  $N/2$  transmission maximizing ‘‘Brewster angles’’ that satisfy

$$\theta_i + \theta_t = (2p + 1)\pi/N, \quad p = 0, 1, \dots, N/2 - 1, \quad (4)$$

while for odd  $N$  we also get Brewster angles that satisfy

$$\theta_i + \theta_t = 2p\pi/N, \quad p = 0, 1, \dots, (N - 1)/2, \quad (5)$$

generating one Brewster angle for BLG and none for MLG. Much like in optics, where a right angle between reflected and transmitted wave vectors quenches reflection (a moving dipole cannot radiate parallel to itself), reflection in BLG is quenched once the reflected pseudospin is orthogonal to the transmitted wave vector at the Brewster angle, preventing a similar back radiation. The observation of a transmission minimum at normal incidence followed by a local maximum at a higher, gate tunable Brewster angle would be a direct experimental signature of AKT.

*Tracking electrons: Corbino disk magnetoresonance.*—Magnetoresistance in ballistic Corbino disk devices is sensitive to the field modulated electron trajectory. When the tightening cyclotron orbits alternately miss the near and far side contact edges, the conductance drops, between magnetic fields  $B_{c1,c2} = \hbar\sqrt{n\pi}/qr_{c1,c2}$ , where the largest tangential orbital radii  $r_{c1,c2} = (r_{\text{contact\_out}} \pm r_{\text{contact\_in}})/2$ , with  $r_{\text{contact\_out}}$  and  $r_{\text{contact\_in}}$  being the outer and inner contact radii. Figure 1(d) shows the measured magnetoresistance for a junctionless MLG Corbino disk device with  $r_{\text{contact\_in}} = 1 \mu\text{m}$ ,  $r_{\text{contact\_out}} = 2.5 \mu\text{m}$ . Experiments (solid line) agree with theory (dashed line), exhibiting a broad plateau up to the expected critical field beyond which the cyclotron radius is smaller than the source-drain separation. For fields higher than  $B_{c2}$ , theory predicts a steep drop in conductance whereas the experiment shows a more gradual response due to a spread in injection angles, shape variations, and nonspecular reflections at the boundaries and within the device.

The dynamics becomes considerably more complex for Corbino disks with a series of concentric  $p$ - $n$  junctions, as needed to see KT or AKT. For a multijunction disk, we adopt a semiclassical numerical ray tracing approach (the  $B$ - $r$  arc equation above) coupled with an analytical

treatment of topology driven KT or AKT transmission [Eq. (3)], with exponential modifications for finite junction width. Electrons are injected from a circular source ( $S$ ) at the center of the Corbino disk with a cosine probability distribution in injection angle [21], after which each electron follows classical equations of motion in the gated region, with quantum phases suppressed by room temperature decoherence. We track each electron, split two ways into fractional counts by the transmission  $T$  and reflection  $1 - T$  at each junction, and by specularly coefficients at each boundary, until they reach a source or a drain, and extract an overall transmission  $\bar{T}$  averaged over all incident angles. We have benchmarked this approach against experiments in the past [2,22]. To ensure no trigonal warping effects [23–26] appear unexpectedly at low bias, a fully atomistic, quantum treatment using nonequilibrium Green's functions is also presented (Supplemental Material [20]) albeit for smaller sizes, as even coarse-grained simulations [27] cannot accommodate self-consistency loops for incoherent scattering within each gated region [28]. Using the transmission count and mode count ( $M$ ), we get the low-bias channel resistance ( $R_{\text{ch}}$ ):

$$M = g_v g_s q(E + V_{\text{ch}})W/\pi\hbar v_F, \quad R_{\text{ch}} = h/q^2 M \bar{T},$$

$$R_T = R_{\text{ch}} + 2R_C. \quad (6)$$

$g_v (= 2)$  is the number of valleys,  $g_s (= 2)$  the number of spins,  $E$  the energy,  $V_{\text{ch}}$  the channel potential calculated from gate voltage and dielectric thickness,  $\hbar$  reduced Planck's constant,  $v_F$  the Fermi velocity,  $W (= 2\pi r_{\text{contact\_in}})$  the circumference of the inner electrode,  $\bar{T}$  the numerically averaged angular transmission per mode, and  $R_C$  the contact resistance extracted from high matched density ( $n$ - $n$ - $n$ ) bias condition.

*KT in Corbino disk MLG devices.*—Figure 2(a) shows a schematic cross section of the MLG Corbino disk device with three circular regions controlled by a bottom and a top gate. The top graphite gate is defined into a Corbino disk shape of inner radius  $r_{\text{in}} = 0.5 \mu\text{m}$  and outer radius  $r_{\text{out}} = 1.5 \mu\text{m}$  by electron beam lithography. The graphene channel is subsequently defined into a slightly larger Corbino disk with radii  $r_{\text{contact\_in}} = 0.25 \mu\text{m}$ ,  $r_{\text{contact\_out}} = 1.8 \mu\text{m}$ . Contact resistance  $R_C = 256 \Omega \mu\text{m}$ . Inner (electron density,  $n_1$ ) and outer ( $n_3$ ) regions are controlled by the bottom gate while the middle region ( $n_2$ ) is controlled by both the top and the bottom gates. In our device, the inner region density  $n_1$  is always equal to the outer region density  $n_3$  resulting in two symmetric  $p$ - $n$  junctions in series between the source and drain. The electrostatic profile of the  $p$ - $n$  junction is controlled by the  $h$ -BN thickness (see Supplemental Material for fabrication and characterization details [20]).

Figures 2(b) and 2(c) show our experimental and simulated magnetoconductance data plotted versus middle

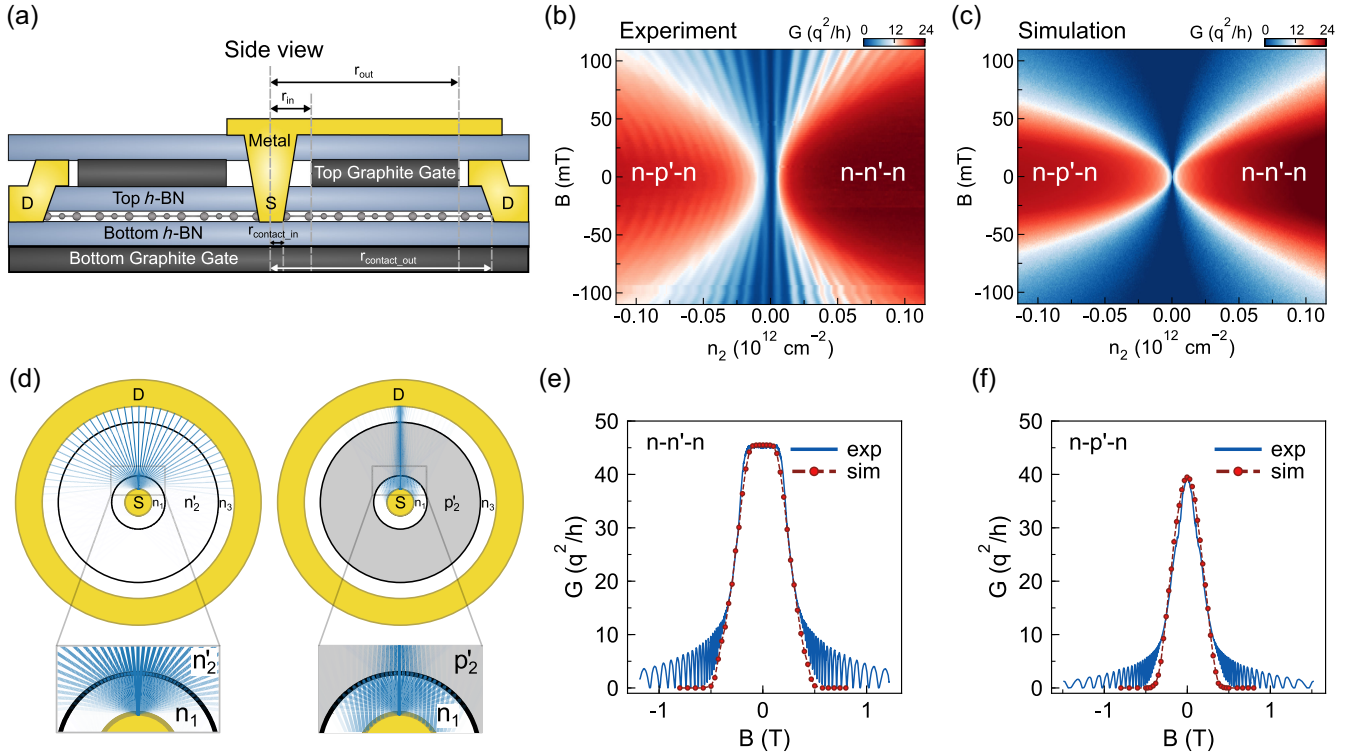


FIG. 2. Electron optics in Corbino disk graphene (monolayer)  $p$ - $n$  junction. (a) Side view of the fabricated Corbino disk monolayer GPNJ device. (b) Experimental and (c) simulated conductance ( $G$ ) color map between inner and outer contact versus magnetic field  $B$  and carrier density  $n_2$ . (d) Top view schematic of Corbino disk monolayer GPNJ device with calculated ray tracing paths (for  $B = 0$  mT) for  $n$ - $n'$ - $n$  and  $n$ - $p'$ - $n$  conditions, with enlarged plots showing sharply collimated electron transmission for the latter. (e)  $G$ - $B$  plot for  $n$ - $n'$ - $n$  versus (f)  $n$ - $p'$ - $n$ , plotted over a wider range of  $B$  fields at  $n_2 = 10^{12}$   $\text{cm}^{-2}$ . Simulations agree with experiments with two separately benchmarked, i.e., no adjustable parameters (see text). Shubnikov–de Haas oscillations inside a gated region must be separately accounted for in simulations, which focus here on low-bias Klein tunneling at the junction. The results show enhanced transmission with  $n$ - $n'$ - $n$  compared to  $n$ - $p'$ - $n$  due to Klein tunneling, as seen in (d) from the multiple transmitting paths across the junction. The  $n$ - $p'$ - $n$  peak is sharp due to the aggressive collimation from Klein tunneling that restricts transmission at  $B = 0$  to normal incidence. A full quantum simulation for a smaller structure with scaled magnetic fields is presented in the Supplemental Material [20].

region electron density  $n_2$  ( $n_1 = n_3 = 1.75 \times 10^{12}$   $\text{cm}^{-2}$ ) and magnetic field. Figure 2(d) shows our ray tracing simulation paths for electrons for  $n$ - $n'$ - $n$  and  $n$ - $p'$ - $n$  junctions, respectively. For  $n$ - $p'$ - $n$ , most of the electrons are filtered out except near zero degree incidences. Figures 2(e) and 2(f) plot line cuts at  $n_2 = -1 \times 10^{12}$   $\text{cm}^{-2}$  to show the conductance variation versus magnetic field for  $n$ - $n'$ - $n$  and  $n$ - $p'$ - $n$  cases, respectively, along with our semiclassical simulation. For  $n$ - $p'$ - $n$ , the peak conductance is smaller than  $n$ - $n'$ - $n$  due to exponential filtering of electrons for higher angles. The conductance profile is also sharper for the  $n$ - $p'$ - $n$  for the same reason. The starting decay point for the  $n$ - $n'$ - $n$  case can be analytically calculated from Ref. [29]. For both of these conductance simulations, our only two nonadjustable fitting parameters are the split length ( $d \sim 37$  nm) of the  $p$ - $n$  junction, benchmarked independently from electrostatic simulations, and the two-probe contact resistance set at  $256 \Omega \mu\text{m}$ , benchmarked from high density experimental resistance. At high fields our semiclassical results miss Shubnikov–de Haas oscillations [30]

from quantum interference within the inner gated region. A full quantum calculation (Supplemental Material, Fig. S1 [20]) restores them.

**AKT in Corbino disk BLG devices.**—While the above results, in particular the sharper and shorter  $n$ - $p'$ - $n$  magnetoconductance peaks versus  $n$ - $n'$ - $n$ , are in quantitative agreement with just two nonadjustable parameters, the maximized conductance at normal incidence is expected for any conventional  $p$ - $n$  junction. AKT in BLG, however, is quite counterintuitive, as it predicts maximum transmission at an intermediate, gate tunable Brewster angle. Figure 3(a) shows a two junction BLG Corbino disk device, with radii  $r_{\text{contact\_in}} = 0.145 \mu\text{m}$ ,  $r_{\text{in}} = 0.5 \mu\text{m}$ ,  $r_{\text{out}} = 2.5 \mu\text{m}$ , and  $r_{\text{contact\_out}} = 3.1 \mu\text{m}$ . Figures 3(c) and 3(d) show the measured magnetoconductance compared to simulations [the contact resistance between channel and source (or drain) is set at  $R_C = 960 \Omega \mu\text{m}$ ]. A prominent local dip is seen in magnetoconductance at low field and attributed to anti-Klein tunneling. The inset in Fig. 3(e) shows the magnetoconductance for a perfectly ballistic structure, zero contact

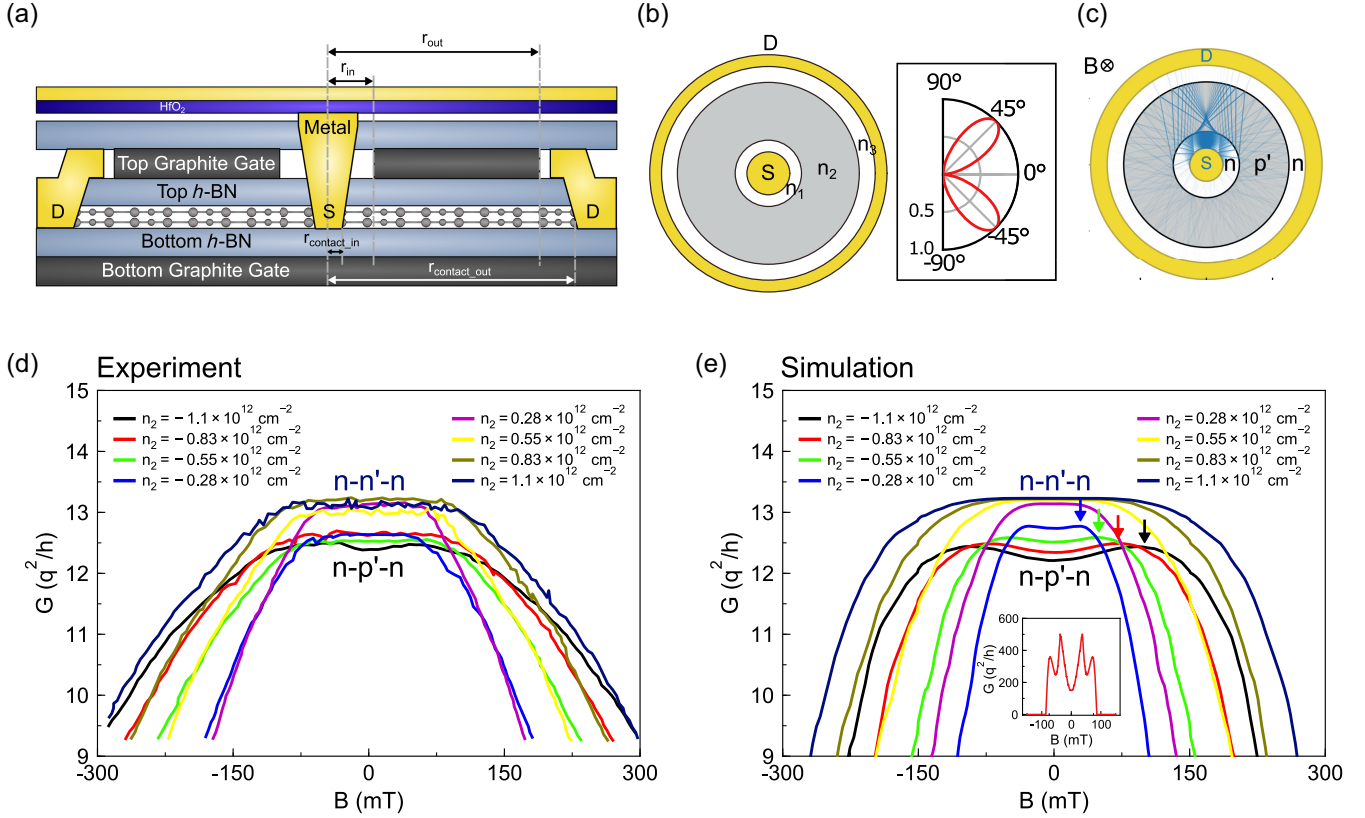


FIG. 3. Electron optics in Corbino disk graphene (bilayer)  $p$ - $n$  junction. (a) Side view of fabricated BLG device structure. (b) Top view and polar plot of angle-dependent transmission across bilayer graphene  $p$ - $n$  junction. (c) Ray tracing paths for  $n$ - $p'$ - $n$  device for  $B = 0$  T. Most of the electrons are filtered across the  $p$ - $n$  junction due to anti-Klein tunneling, compared to monolayer graphene [Fig. 2(d)]. (d) Experimental versus (e) simulated  $G$ - $B$  plot, simulations including scattering (see text). A pronounced dip is seen at zero field in the magnetoconductance plot corresponding to quenching of the transmission at normal incidence, as expected for BLG AKT (Fig. 1, blue dashed line). The inset in (e) shows a simulation with minimal scattering, where the peaks are more pronounced. Arrows show analytical predictions [Eq. (7)] of the maximizing fields corresponding to the Brewster angle, migrating out to higher fields with increasing doping density. A full quantum simulation for a smaller structure with scaled magnetic fields is presented in the Supplemental Material [20].

resistance, and electron density set to  $n_1 = 2.6 \times 10^{12} \text{ cm}^{-2}$  and  $n_2 = -3.2 \times 10^{12} \text{ cm}^{-2}$ , while the main plot shows it in the presence of scattering. We use an average elastic scattering length of 300 nm and a nonspecular scattering at each interface extracted from a random Gaussian distribution function with standard deviation  $\sigma$  of  $20^\circ$  (the scattering length subsumes in it effects from geometric nonidealities such as nonconcentric disks or trigonal deformations). We would like to emphasize that while the dip itself is seen prominently on one curve, it happens for parameters where we expect the largest dip, accounting for disorder. Furthermore, we see an abundance of additional curves with robust plateaus that are qualitatively different from Fig. 2 and similar to the simulation results in Fig. 3(e), including their involved field and density-dependent evolution. We argue that the evolution of the entire family of magnetoresistance curves and their uncharacteristic shapes including a low-field dip with adjoining shoulders, consistent with numerical simulations (semiclassical above, full quantum in the Supplemental Material [20]), consistent with

simple equations [arrow locations in Fig. 3(e) herein and Fig. S2 [20]), directly arise from anti-Klein tunneling in BLGs. While we expect higher doping to lead to more prominent dips, this would require a different device design to avoid associated dielectric breakdown.

Figure 3(c) shows simulated ray tracing paths for electrons for  $n$ - $p'$ - $n$ , where most of the electrons are filtered out near normal incidence. For the Brewster angle  $\theta_{\text{AKT}} = \tan^{-1}(n_1/n_2)$  ( $n_i$  set by the local gate voltage  $V_{Gi}$ ), where transmitted and reflected electrons are orthogonal, the conductance is locally maximized. The corresponding magnetic field is given by

$$B_{\text{peak}} = \hbar \sqrt{\pi n_2} / q r_{\text{AKT}},$$

$$r_{\text{AKT}} = (r_{\text{out}}^2 - r_{\text{in}}^2) / 2 r_{\text{out}} \sin \theta_{\text{AKT}}. \quad (7)$$

In Fig. 3(e), we mark out with colored arrows the magnetic field values ( $B_{\text{AKT}}$ ) corresponding to the peak conductances, i.e., Brewster angles, as obtained from

Eq. (7). We see an excellent match between these analytical results and the numerical peak positions, and a good qualitative agreement, especially on the peak migration with doping, compared with experiment [Fig. 3(d)] and consistent with AKT expectations.

*Conclusion.*—Nontrivial topological properties of materials have proved critical for their discovery and classification, as well as arguably improving their overall carrier mobility, although these advantages are fundamentally offset by low drivability including carrier density, and poor integrability, including contact resistance. Topology also controls the evolution of electron wave function around the Fermi surface, imposing symmetry restrictions on transmission across barriers. This Letter demonstrates direct experimental evidence of universal KT and AKT across edgeless (Corbino disk)  $p$ - $n$ - $p$  MLG and BLG junctions. The physics gets richer with increasing layer number, with alternating KT and AKT signatures with multiple Brewster angles, albeit over smaller voltage ranges. Another direction is to look at hybrid bandpass structures (mono and bilayer laterally stacked), potentially eliminating low angle electrons with AKT and high angles with KT. Since barriers can be electrically gated, this opens a rich field of *pseudospintronics*, unconventional classical computing with topological materials, such as through the deliberate engineering of gate tunable transmission functions [4–6].

This work was supported by the Semiconductor Research Corporation's Nanoelectronics Research Initiative (NRI) Center for Institute for Nanoelectronics Discovery and Exploration (INDEX). Device fabrication and measurement was supported by the Columbia MRSEC on Precision-Assembled Quantum Materials (PAQM)—DMR-2011738.

\*Corresponding author: me5vp@virginia.edu

Present address: Intel Corporation, Santa Clara, California 95054, USA.

†Present address: Department of Physics, Cornell University, Ithaca, New York 14850, USA.

- [1] V. V. Cheianov, V. Fal'ko, and B. Altshuler, *Science* **315**, 1252 (2007).
- [2] S. Chen, Z. Han, M. M. Elahi, K. M. Habib, L. Wang, B. Wen, Y. Gao, T. Taniguchi, K. Watanabe, J. Hone, A. W. Ghosh, and C. R. Dean, *Science* **353**, 1522 (2016).
- [3] V. V. Cheianov and V. I. Fal'ko, *Phys. Rev. B* **74**, 041403(R) (2006).
- [4] R.-N. Sajjad and A. W. Ghosh, *ACS Nano* **7**, 9808 (2013).
- [5] K. Wang, M. M. Elahi, L. Wang, K. M. Habib, T. Taniguchi, K. Watanabe, J. Hones, A. W. Ghosh, G.-H. Lee, and P. Kim, *Proc. Natl. Acad. Sci. U.S.A.* **116**, 6575 (2019).
- [6] Y. Tan, M. M. Elahi, H.-Y. Tsao, K. M. Habib, N. S. Barker, and G. A. W., *Sci. Rep.* **7**, 9714 (2017).
- [7] R. N. Sajjad, S. Sutar, J.-U. Lee, and A. W. Ghosh, *Phys. Rev. B* **86**, 155412 (2012).
- [8] G.-H. Lee, G.-H. Park, and H.-J. Lee, *Nat. Phys.* **11**, 925 (2015).
- [9] N. Stander, B. Huard, and D. Goldhaber-Gordon, *Phys. Rev. Lett.* **102**, 026807 (2009).
- [10] Z. Zhang, Y. Feng, F. Li, S. Koniakhin, C. Li, F. Liu, Y. Zhang, M. Xiao, G. Malpuech, and D. Solnyshkov, *Phys. Rev. Lett.* **129**, 233901 (2022).
- [11] C. Gutierrez, L. Brown, C.-J. Kim, J. Park, and A. N. Pasupathy, *Nat. Phys.* **12**, 1069 (2016).
- [12] S. Lee, V. Stanev, X. Zhang, D. Stasak, J. Flowers, J. S. Higgins, S. Dai, T. Bloom, X. Pan, V. M. Yakovenko, J. Paglione, R. L. Greene, V. Galitski, and I. Takeuchi, *Nature (London)* **570**, 344 (2019).
- [13] M. I. Katsnelson, K. S. Novoselov, and A. K. Geim, *Nat. Phys.* **2**, 620 (2006).
- [14] R. Du, M.-H. Liu, J. Mohrmann, F. Wu, R. Krupke, H. v. Löhneysen, K. Richter, and R. Danneau, *Phys. Rev. Lett.* **121**, 127706 (2018).
- [15] B. Schmidt, K. Bennaceur, S. Bilodeau, G. Gervais, L. Pfeiffer, and K. West, *Solid State Commun.* **217**, 1 (2015).
- [16] J. Yan and M. S. Fuhrer, *Nano Lett.* **10**, 4521 (2010).
- [17] Y. Zhao, P. Cadden-Zimansky, F. Ghahari, and P. Kim, *Phys. Rev. Lett.* **108**, 106804 (2012).
- [18] E. C. Peters, A. Giesbers, M. Burghard, and K. Kern, *Appl. Phys. Lett.* **104**, 203109 (2014).
- [19] M. Kumar, A. Laitinen, and P. Hakonen, *Nat. Commun.* **9**, 2776 (2018).
- [20] See Supplemental Material at <http://link.aps.org/supplemental/10.1103/PhysRevLett.132.146302> for experimental method and full quantum simulation of MLG and BLG.
- [21] L. W. Molenkamp, A. A. M. Staring, C. W. J. Beenakker, R. Eppenga, C. E. Timmering, J. G. Williamson, C. J. P. M. Harmans, and C. T. Foxon, *Phys. Rev. B* **41**, 1274 (1990).
- [22] R. N. Sajjad, S. Sutar, J. U. Lee, and A. W. Ghosh, *Phys. Rev. B* **86**, 155412 (2012).
- [23] C. G. Péterfalvi, L. Oroszlány, C. J. Lambert, and J. Cserti, *New J. Phys.* **14**, 063028 (2012).
- [24] S. Milovanović, M. Ramezani Masir, and F. Peeters, *J. Appl. Phys.* **114**, 113706 (2013).
- [25] L. Seemann, A. Knothe, and M. Hentschel, *Phys. Rev. B* **107**, 205404 (2023).
- [26] P. A. Maksym and H. Aoki, [arXiv:2306.10235](https://arxiv.org/abs/2306.10235).
- [27] K. M. Habib, R. N. Sajjad, and A. W. Ghosh, *Appl. Phys. Lett.* **108**, 113105 (2016).
- [28] A. Ghosh, *Nanoelectronics—A Molecular View* (World Scientific, Singapore, 2016).
- [29] G. Kirczenow, *J. Phys. Condens. Matter* **6**, L583 (1994).
- [30] Z. Tan, C. Tan, L. Ma, G. T. Liu, L. Lu, and C. L. Yang, *Phys. Rev. B* **84**, 115429 (2011).